



Original Article

Synthesis and Luminescence Properties of ZnO: Eu³⁺ Nanopowders

Trinh Thi Loan*, Cao Thi Huyen Trang, Vu Hoang Huong

VNU University of Science, 334 Nguyen Trai, Thanh Xuan, Hanoi, Vietnam

Received 10th March 2026

Revised 6th April 2025; Accepted 5th May 2026

Abstract: The effect of Eu³⁺ doping on the structural and photoluminescence properties of zinc oxide (ZnO) nanopowders synthesized via the sol-gel method was investigated. The samples were characterized using powder X-ray diffraction (XRD), Raman spectroscopy, photoluminescence (PL), and photoluminescence excitation (PLE) spectroscopy. XRD results revealed that samples with low Eu³⁺ concentration exhibited a single hexagonal wurtzite phase, whereas higher Eu³⁺ concentrations consisted of ZnO and Eu₂O₃ phases. The results calculated from XRD indicate that a small amount of Eu³⁺ ions has been successfully doped into the ZnO host lattice. The Raman spectra of Eu³⁺ doped ZnO reveal significant modifications in vibrational behavior arising from Eu³⁺ incorporation. PL spectrum of the undoped ZnO sample exhibits peaks in both the ultraviolet (UV) and visible regions. The UV emission peaks arise from electron recombination near the band gap, while the visible emission peaks are attributed to oxygen vacancies (V_O^0, V_O^+, V_O^{++}). The sharp direct 4f-4f excitation and emission lines of Eu³⁺ were observed in the PLE and PL spectra, respectively. The energy transfer from the ZnO host to Eu³⁺ ions is found.

Keywords: Sol-gel, ZnO:Eu³⁺ nanopowders, Raman, photoluminescence.

1. Introduction

Zinc oxide (ZnO) is an important and attractive II-VI semiconductor due to its wide direct band gap (approximately 3.37 eV) and a large exciton binding energy (60 meV). Because of their low cost, low toxicity, biocompatibility, superior chemical and unique optical properties, ZnO nanomaterials are used in a wide range of applications, including optics [1, 2], electronics [3], biology [4], and environmental protection [5]. Under appropriate excitation conditions, ZnO exhibits two main emission bands, one at

* Corresponding author.

E-mail address: loan.trinhthi@gmail.com

<https://doi.org/10.25073/2588-1124/vnumap.5125>

around 380 nm, attributed to near-band-edge emission, and a broader band in 450–800 nm, associated with intrinsic defect emission [5, 6]. Rare-earth doping of ZnO (ZnO:RE) can expand its optical and electronic properties by altering defects and electron transport. The 4f electronic transitions of RE ions introduce characteristic visible emission lines and can influence the electronic structure, thereby enhancing photoconductivity and charge-carrier control. As a result, ZnO:RE materials are promising candidates for applications in light-emitting diodes, sensors, and UV photodetectors [7]. In this study, ZnO:Eu³⁺ nanopowders were synthesized via the sol–gel method because of its simplicity, low cost, and suitability for large-scale production. This synthesis route provides molecular-level homogeneity, ensuring uniform dispersion of dopant ions within the ZnO host lattice. The influence of Eu³⁺ doping concentration on the structural, PL, and PLE properties of ZnO:Eu³⁺ nanopowders is systematically investigated.

2. Experimental

ZnO:Eu³⁺ nanopowders were prepared via the sol–gel method. First, 0.2 g of (CH₂CHOH)_n was dissolved in 20 mL of distilled water at room temperature under magnetic stirring until a clear solution was obtained. Subsequently, 2 g of Zn(O₂CCH₃)₂ was added to the solution and the mixture was stirred for 30 min. An aqueous solution of Eu(NO₃)₃ (0.2 M) was then introduced to obtain Eu³⁺ doping concentrations of 0.0, 0.1, 0.5, 1.0, 3.0, and 6.0 mol%. The corresponding samples were denoted as S0, S1, S2, S3, S4, and S5, respectively. The mixtures were continuously stirred and heated at 80 °C until the solvent evaporated and a transparent gel was formed. The gel was then dried at 100 °C for 24 h. Finally, the dried products were annealed at 650 °C for 5 h to obtain ZnO:Eu³⁺ nanopowders.

The crystalline structure of ZnO:Eu³⁺ nanopowders was studied by an Empyrean X-ray diffractometer (XRD), using Cu-Kα₁ irradiation ($\lambda = 1.54056 \text{ \AA}$). SEM images were obtained using a Thermo Scientific Apreo 2S scanning electron microscope. Raman spectra were obtained using a micro-Raman spectrophotometer, LabRAM HR 800 (HORIBA JobinYvon), with an excitation wavelength of 632.8 nm. Photoluminescence (PL) and photoluminescence excitation (PLE) spectra were recorded at room temperature using a Fluorolog FL3-22 spectrofluorometer (Jobin Yvon Spex) with a 450 W xenon lamp as the excitation source.

3. Results and Discussion

3.1. Morphology and Structure Characterization

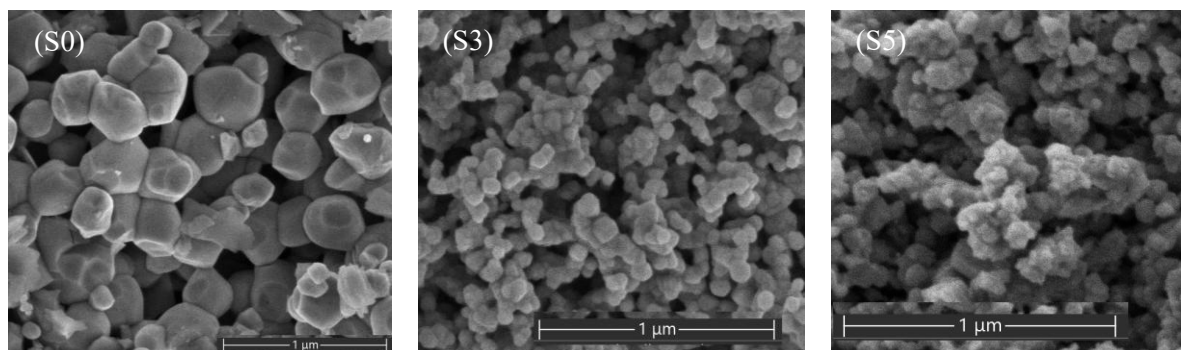


Figure 1. SEM images of S0, S3, and S5 samples.

The SEM images of S0, S3, and S5 samples are shown in Fig. 1. It can be seen that the size of the particles decreases with increasing Eu^{3+} content. The undoped S0 sample's irregular aggregated morphology has a relative particle diameter in the range of 100 - 350 nm, whereas the S3 sample has a diameter in the 40 - 70 nm range, and the S5 sample has a diameter in the 20 - 40 nm range.

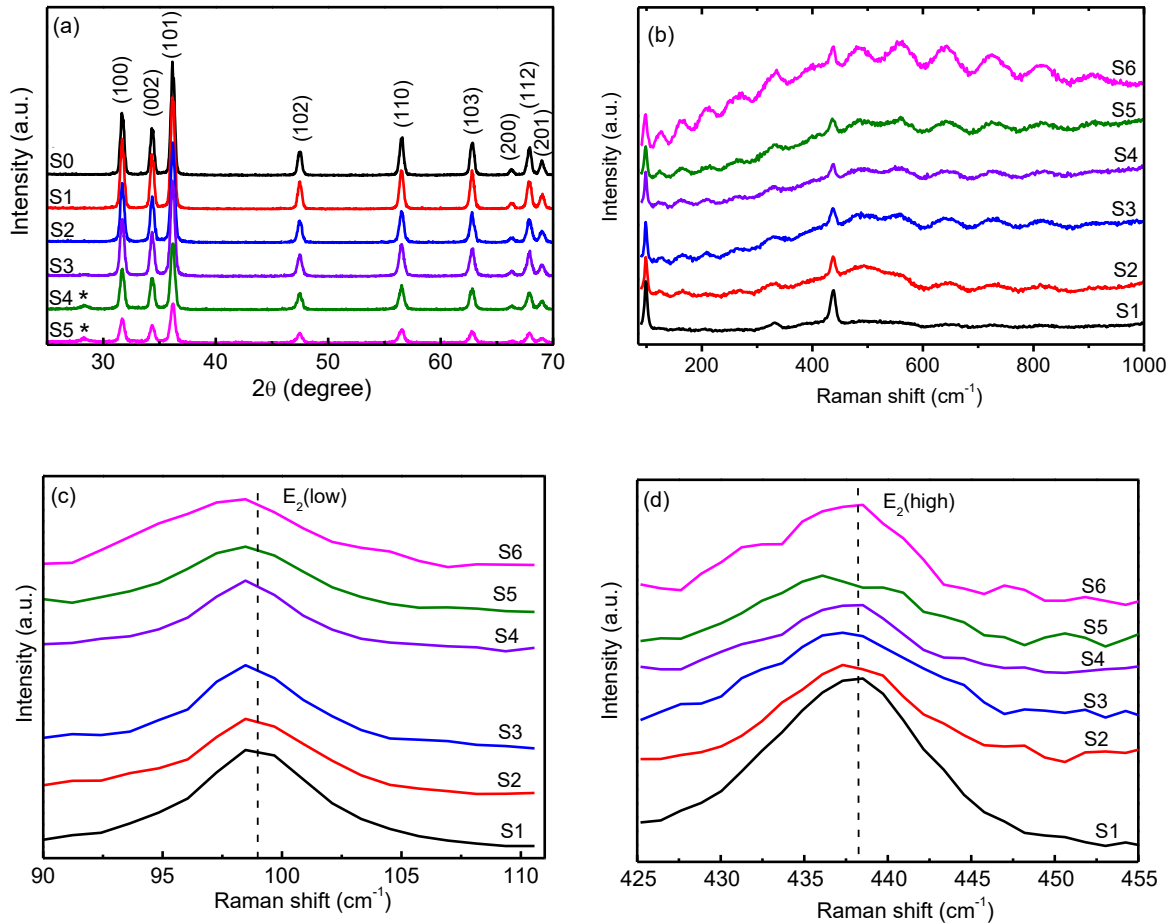


Figure 2. XRD patterns (a), Raman spectra (b), enlarged area for $E_2(\text{low})$ (c) and $E_2(\text{high})$ (d) of S0, S1, S2, S3, S4 and S5 samples.

Fig. 2(a) presents the XRD patterns recorded in the $25 \div 70^\circ$ range of the S0-S5 samples. XRD results indicate well-defined diffraction peaks with high crystallinity, characteristic of hexagonal wurtzite ZnO structure (JCPDS No. 36-1451). No additional peak was detected in S1, S2 and S3 samples, thus suggesting homogeneous dispersion of dopant in ZnO host. However, a weak peak appears at about 28.28° for sample S4 and grows further in intensity for S5, which has been ascribed to (222) crystal planes phase of Eu_2O_3 (JCPDS No. 86-2476). It indicates that a small proportion of Eu_2O_3 is separated from the ZnO host. Notably, the XRD peaks of $\text{ZnO}:\text{Eu}^{3+}$ are slightly broader and weaker in intensity compared to those of ZnO, indicating that the incorporation of Eu^{3+} ions inhibits the growth of ZnO. The inhibition of crystallite growth was also observed in doped ZnO with other rare earths, such as Er^{3+} [8] and Sm^{3+} [9]. The grain size of the crystallites, interplanar spacing, and lattice parameters of all samples were calculated using the formula given below:

$$D = \frac{k\lambda}{\beta \cos\theta} [10], d = \frac{\lambda}{2\sin\theta} [11] \text{ and } \frac{1}{d^2} = \frac{4(h^2+k^2+hk)}{3a^2} + \frac{l^2}{c^2}$$

where: D is the mean crystallite size, K is the shape factor taken as 0.89, λ is the wavelength of the incident beam, β is the full width at half maximum and θ is the Bragg angle. The results were calculated using the most intense diffraction peaks of ZnO, corresponding to the (100), (002), and (101) planes, as shown in Table 1. Compared to the undoped ZnO sample, the lattice parameters of ZnO:Eu³⁺ are slightly expanded due to the larger ionic radius of Eu³⁺ (0.95 Å) compared to that of Zn²⁺ (0.74 Å) [12]. This result indicates that a small amount of Eu³⁺ ions has been successfully doped into the crystal lattice of ZnO host. Some previous studies have shown that Eu³⁺ does not readily substitute for Zn²⁺ tetrahedral sites in the wurtzite-type structure, leading to Eu³⁺ occupying interstitial positions or forming surface clusters [12, 13].

Table 1. XRD parameters and average size of crystalline grains for S0, S1, S2, S3, S4 and S5.

Sample name	2 θ (°)	d- spacing (Å)	FWHM (°)	Average crystalline size D (nm)	Lattice parameter (Å)
S0	31.689	2.8213	0.3455	24.1	a = 3.2570 ± 0.0007 c = 5.2128 ± 0.0039
	34.352	2.6033	0.3418		
	36.179	2.4808	0.3461		
S1	31.684	2.8217	0.3552	23.5	a = 3.2574 ± 0.0008 c = 5.2128 ± 0.0042
	34.350	2.6086	0.3486		
	36.175	2.4810	0.3551		
S2	31.690	2.8312	0.3601	23.1	a = 3.2569 ± 0.0007 c = 5.2127 ± 0.0040
	34.353	2.6083	0.3535		
	36.180	2.4807	0.3671		
S3	31.682	2.8219	0.3755	22.1	a = 3.2570 ± 0.0007 c = 5.2128 ± 0.0039
	34.349	2.6086	0.3721		
	36.171	2.4812	0.3816		
S4	31.688	2.8213	0.3764	22.1	a = 3.2577 ± 0.0007 c = 5.2134 ± 0.0039
	34.356	2.6081	0.3735		
	36.177	2.4809	0.3792		
S5	31.688	2.8213	0.4124	20.6	a = 3.2573 ± 0.0006 c = 5.2129 ± 0.0032
	34.355	2.6082	0.3932		
	36.179	2.4807	0.4031		

In addition, Raman spectroscopy was used to complement the structural characterization of the synthesized samples, and the spectra are shown in Fig. 2(b). The peak positions are summarized in Table 2. The Raman spectrum of the S0 sample exhibits peaks at 98.6, 164, 207, 333, 390, 438.2, 495, 561, 650, 728, and 813 cm⁻¹. Our results are consistent with previous Raman studies [14-19]. Two very intense, sharp peaks at 98.6 and 438.2 cm⁻¹ belong to the E₂(low) and E₂(high) modes of ZnO. The E₂(low) mode is related to the vibration of the Zn lattice, while the E₂(high) mode is attributed to the vibration of the O lattice [14-19]. The Raman peak located at about 164 cm⁻¹ was assigned to the transverse acoustic (TA) phonons around the K point of the Brillouin zone [17]. The peak at 207 cm⁻¹ can be attributed to 2E₂(low) and 2TA overtones L-M and H [14, 18]. The peak, which appears at 333 cm⁻¹, is ascribed to the difference E₂(high)-E₂(low) [14, 15, 18]. The peaks at 390 and 561 cm⁻¹ can be attributed to E₁(TO) and A₁(LO), respectively [14, 18]. The peak at 495 cm⁻¹ contains contributions from the 2B₁(low) mode at the Γ point of the Brillouin zone and the 2LA overtones at the L, M, H and K points [14, 18]. The combination of acoustic and optical modes appears at 650 cm⁻¹ [14, 18]. The peaks at 728 and 813 cm⁻¹ can correspond to the second-order Raman modes with A₁ symmetry [14].

Table 2. The wavenumbers of Raman-active vibrations observed in S0, S1, S2, S3, S4 and S5 samples.

Process	Brillouin zone points	Wavenumbers (cm ⁻¹)						Ref. [14]
		S0	S1	S2	S3	S4	S5	
E ₂ (low)	Γ	98.6	98.5	98.5	98.4	98.4	98.3	99
TA	M	-	124	126	126	124	126	
TA	K	164	165	163	167	165	164	
2TA, 2E ₂ (low)	L, M, H; Γ	207	206	206	210	213	213	208
B ₁ (high)- B ₁ (low)	Γ	-	264	265	265	269	268	284
E ₂ (high)-E ₂ (low)	Γ	333	330	326	331	331	332	333
E ₁ (TO)	Γ	390	394	397	403	403	406	410
E ₂ (high)	Γ	438.2	437.8	437.3	437.2	436.5	436.6	433
2B ₁ (low); 2LA	Γ; L, M, H, K	495	494	490	490	483	483	536
A ₁ (LO)	Γ	561	557	560	563	560	556	574
E ₁ (TA)+E ₁ (LO), E ₂ (TA)+E ₂ (LO)	L, H	650	644	644	639	642	641	657
A ₁ (LO)+A ₁ (TO)	L-M	728	731	728	728	727	726	723
A ₁ (LO)+A ₁ (TO)	L, M	813	813	815	818	816	818	812
A ₁ (2TO)	L-M-K-H	-	-	-	-	910	910	980

Compared to the undoped sample, the Raman spectra of Eu³⁺ doped ZnO reveal significant modifications in vibrational behavior arising from Eu incorporation. As shown in Fig. 2(c,d), the intensities of both the E₂(low) and E₂(high) modes decrease markedly with increasing Eu³⁺ concentration. Moreover, increasing Eu³⁺ doping leads to asymmetrical broadening and a shift toward lower wavenumbers of these modes. Two additional peaks were observed in all Eu-doped ZnO samples, located at approximately 124 cm⁻¹ and 264 cm⁻¹. Moreover, an additional peak at 910 cm⁻¹ was detected in the 3.0 and 6.0 mol% Eu-doped ZnO samples. The peak at about 124 cm⁻¹ was assigned to the transverse acoustic (TA) phonons around the M point of the Brillouin zone [17]. The peak appearing at approximately 264 cm⁻¹ is attributed to the difference mode B₁(high)–B₁(low) [14]. The peak at 910 cm⁻¹ could be attributed to the A₁(2TO) overtone modes at the L, M, H, and K points [14]. Another noteworthy feature is that all Raman modes, except for the E₂(low) and E₂(high) modes, exhibit increased intensity with increasing Eu³⁺ impurity concentration. It is well known that the E₂(low) mode is influenced by Zn²⁺ interstitial defects and E₂(high) by O₂ vacancies [19]. The A₁(LO) and E₁(LO) modes are usually associated with the defect Zn²⁺ interstitial and O²⁻ vacancy in ZnO lattice [19]. In addition, according to the Raman selection rule, the B₁ modes are generally inactive in Raman spectra [14-18]. These modifications indicate that substitution at Zn²⁺ sites by Eu³⁺ ions, accompanied by the breakdown of translational crystal symmetry, the formation of O²⁻ vacancies, and the Zn²⁺ interstitial, constitute the predominant disorder-related defects in Eu³⁺ doped ZnO samples.

3.2. Luminescence Characterization

Fig. 3(a) shows the photoluminescence excitation (PLE) spectra monitored at 510 nm of S0-S5 samples. In each spectrum, a high excitation band at 285 – 395 nm with a maximum at 370 nm (3.35 eV) was observed. This excitation band is attributed to electronic transitions involving the valence band, conduction band, and intrinsic defect levels of the ZnO host lattice [20]. The intensity of this excitation band gradually decreases with increasing Eu³⁺ concentration. This behavior may be associated with changes in the defect chemistry of the Eu-doped ZnO system. Fig. 3(b) presents the PL spectra of the S0-S5 samples in the range of 410-710 nm, with an excitation wavelength of 370 nm, corresponding to

the wavelength of the most intense peak in the PLE spectrum. The PL spectrum of the S0 sample displays three distinct emission peaks at approximately 510, 610, and 665 nm, among which the 610 nm emission exhibits the highest intensity. These peaks are attributed to radiative transitions from the conduction band to deep-level defect states related to deep-level neutral oxygen vacancies (V_O), oxygen vacancies single charge (V_O^+) and oxygen vacancies double charge (V_O^{++}), respectively [21]. Interestingly, the intensity of the deep-level defect emissions associated with the ZnO host lattice decreases markedly in the Eu-doped ZnO samples, accompanied by the appearance of sharp PL peaks at 578, 592, and 615 nm. These emissions are attributed to the transitions from the excited 5D_0 level to the 7F_0 , 7F_1 , and 7F_2 levels of Eu^{3+} ($4f^6$ configuration), respectively [22, 23]. This observation confirms the energy transfer from the ZnO host to Eu^{3+} ions.

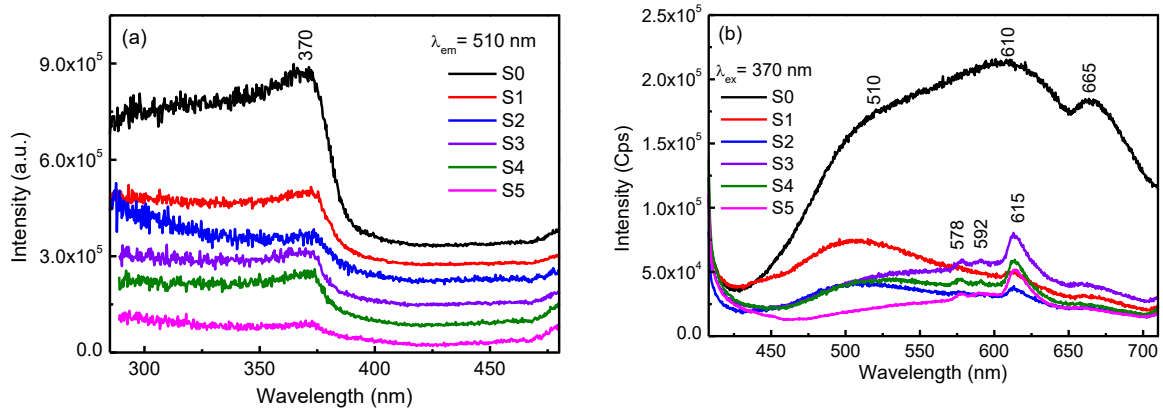


Figure 3. PLE (a) and PL (b) spectra of S0, S1, S2, S3, S4 and S5 samples.

Fig. 4(a) presents the PL spectra of the S0–S5 samples under excitation at 335 nm. The excitation energy (3.7 eV) exceeds the band gap energy of ZnO (3.4 eV), enabling the excitation of electrons from the valence band to the conduction band and to defect-related states within the band gap. In addition to the visible emission band, the UV emission peak with a maximum at 383 nm was observed. This peak is a near-band-edge (NBE) recombination and is considered a characteristic emission of ZnO [24]. A careful examination of the UV region of the PL spectra reveals a gradual decrease in the intensity of the 383 nm peak with increasing Eu^{3+} concentration. In addition, a weak emission peak at 398 nm was also observed. The 398 nm peak is attributed to electron transitions from a localized energy level slightly below the conduction band to the valence band [24]. Fig. 4(b) presents the PLE spectra of the S3 sample, recorded by monitoring emission wavelengths at 578, 592, 615, and 665 nm. The PLE spectrum of the S3 sample monitored at 510 nm is also presented for comparison. In addition to the broad excitation band related to the ZnO host, five sharp direct 4f–4f excitation lines of Eu^{3+} were observed in the excitation spectra. Specifically, the sharp lines at 394, 415, 464, 531 and 578 nm correspond to electron transitions from the ground state 7F_0 to the different excited states 5L_6 , 5D_3 , 5D_2 , 5D_1 and 5D_0 of the Eu^{3+} ions, respectively [25]. In particular, the appearance of a broad UV excitation band associated with the ZnO host in the selective PLE spectra monitored at the $^5D_0 \rightarrow ^7F_1$ (592 nm) and $^5D_0 \rightarrow ^7F_2$ (615 nm) emissions indicates an indirect excitation mechanism via energy transfer from the ZnO host to Eu^{3+} ions. Based on the PL and PLE results, the energy transfer process can be described as follows. Upon UV excitation, the ZnO host absorbs incident photons, promoting electrons from the valence band to the conduction band through direct band-to-band transitions. The excited electrons subsequently recombine with holes in the valence band and deep-level defect states, inducing emissions at 383, 510, 610, and

665 nm. Part of this emitted energy is then transferred non-radiatively to nearby Eu^{3+} ions, promoting their electrons from the ground state to excited states and resulting in the characteristic Eu^{3+} emissions.

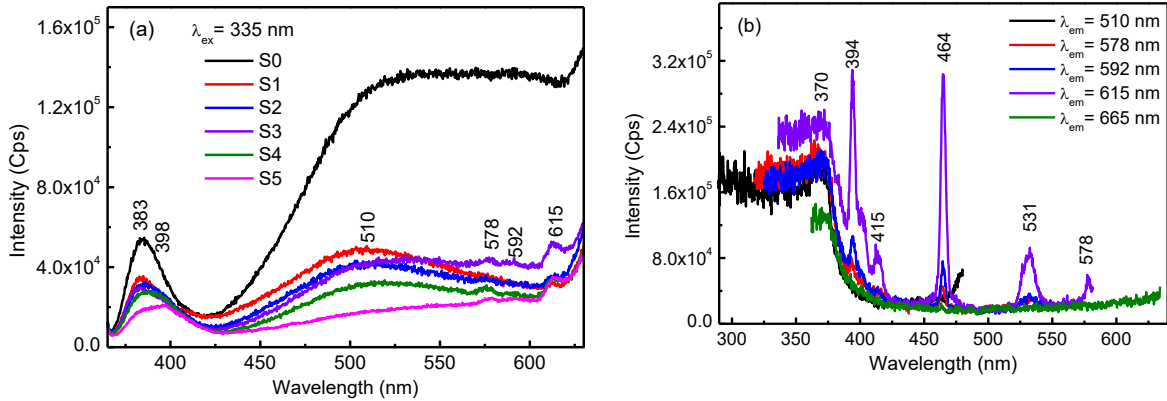


Figure 4. PL spectra under excitation wavelengths 335 nm of S1–S5 samples (a) and PLE spectra monitored at different wavelengths of the S3 sample (b).

The PL spectra of the S1–S5 samples excited at 394 and 464 nm are presented in Fig. 5(a-b). The emission spectra under both excitation wavelengths are similar, consisting of sharp peaks located at 578 nm ($^5\text{D}_0 \rightarrow ^7\text{F}_0$), 592 nm ($^5\text{D}_0 \rightarrow ^7\text{F}_1$), 615 nm ($^5\text{D}_0 \rightarrow ^7\text{F}_2$), 655 nm ($^5\text{D}_0 \rightarrow ^7\text{F}_3$), and 692–704 nm ($^5\text{D}_0 \rightarrow ^7\text{F}_4$), which are characteristic transitions of Eu^{3+} ions. The optimal doping concentration was determined to be 1.0 mol% (S3 sample). A further increase in Eu^{3+} concentration resulted in concentration quenching, which can be attributed to enhanced non-radiative energy transfer among neighboring Eu^{3+} ions. It is well known that the PL intensity ratio ($^5\text{D}_0 \rightarrow ^7\text{F}_2$)/($^5\text{D}_0 \rightarrow ^7\text{F}_1$) is an important parameter for evaluating the asymmetry of Eu^{3+} sites, reflecting the proportion of Eu^{3+} ions occupying non-centrosymmetric versus centrosymmetric environments [26]. The electric dipole transition ($^5\text{D}_0 \rightarrow ^7\text{F}_2$), corresponding to the emission peak at 615 nm, is highly sensitive to local structural changes and is widely used as a spectroscopic probe. In contrast, the $^5\text{D}_0 \rightarrow ^7\text{F}_1$ transition at 592 nm is a magnetic dipole transition and is relatively insensitive to site symmetry. In our samples, Eu^{3+} ions are located in a low-symmetry crystal field; therefore, the emission spectrum is dominated by the intense red emission at 615 nm arising from the $^5\text{D}_0 \rightarrow ^7\text{F}_2$ transition.

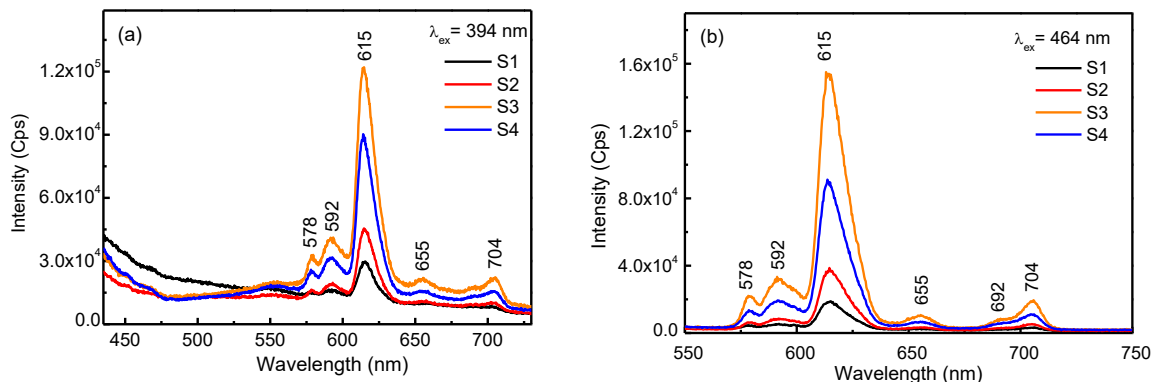


Figure 5. PL spectra under excitation wavelengths 394 nm (a) and 464 nm (b) of S1–S5 samples.

4. Conclusion

The effects of Eu^{3+} doping on the structural and photoluminescence properties of $\text{ZnO}:\text{Eu}^{3+}$ nanopowders were investigated. XRD results confirm that all samples possess a hexagonal wurtzite structure, while a weak secondary phase attributed to Eu_2O_3 appears at higher Eu^{3+} concentrations (3 and 6 mol%). XRD and Raman analyses reveal that the incorporation of Eu^{3+} ions at Zn^{2+} sites induces lattice disorder, leading to the formation of O^{2-} vacancies and Zn^{2+} interstitials. The PL spectra exhibit near-band-edge emission, defect-related emissions, and characteristic Eu^{3+} transitions from the $^5\text{D}_0$ excited state to the $^7\text{F}_j$ ($j = 0-4$) levels. Due to the low-symmetry crystal field surrounding Eu^{3+} ions, the emission is dominated by a strong red band at 615 nm corresponding to the $^5\text{D}_0 \rightarrow ^7\text{F}_2$ transition. These results show that $\text{ZnO}:\text{Eu}^{3+}$ nanopowders are promising candidates for orange-red phosphors in pc-LED applications.

References

- [1] R. Sha, A. Basak, P. C. Maity, S. Badhulika, ZnO Nano-structured Based Devices for Chemical and Optical Sensing Applications, *Sens. Actuator Rep.*, Vol. 4, 2022, pp. 100098, <https://doi.org/10.1016/j.snr.2022.100098>.
- [2] E. Moya, J. H. Kim, J. Kim, J. Jang, ZnO Nanoparticles for Quantum-Dot-Based Light-Emitting Diodes, *ACS Appl. Nano Mater.*, Vol. 3, No. 6, 2020, pp. 5203-5211, <https://doi.org/10.1021/acsanm.0c00639>.
- [3] D. Buckley, A. Lonergan, C. O'Dwyer, Review-ZnO-based Thin Film Metal Oxide Semiconductors and Structures: Transistors, Optoelectronic Devices and Future Sustainable Electronics, *J. Solid State Sci. Technol.*, Vol. 14, No. 1, 2025, pp. 015001, <https://doi.org/10.1149/2162-8777/ada3a2>.
- [4] S. Dey, D. Mohanty, N. Divya, V. Bakshi, A. Mohanty, D. Rath, S. Das, A. Mondal, S. Roy, R. Sabui, A critical Review on Zinc Oxide Nanoparticles: Synthesis, Properties and Biomedical Applications, *Intell. Pharm.*, Vol. 3, No. 1, 2025, pp. 53-70, <https://doi.org/10.1016/j.ipha.2024.08.004>.
- [5] O. M. Ramirez, M. Cornet, D. P. Ospina, M. M. Albor, M. Millan, E. M. Vargas, M. Tirado, D. Comedi, Environmental-related Applications of ZnO Nanopowders: Photocatalytic Activity and Photoluminescence Response to Ethanol, *Environmental-nanotechnology-monitoring & Management, Environ. Nanotechnol. Monit. Manag.*, Vol. 21, 2024, pp. 100947, <https://doi.org/10.1016/j.enmm.2024.100947>.
- [6] M. Benamara, J. Massoudi, H. Dahman, A. Ly, E. Dhahri, M. Debliquy, L. El Mir, D. Lahem, Study of Room Temperature NO_2 Sensing Performances of ZnO_{1-x} ($x = 0, 0.05, 0.10$). *Appl. Phys. A*, Vol. 128, No. 31, 2022, <https://doi.org/10.1007/s00339-021-05172-7>.
- [7] S. Sood, P. Kumar, I. Raina, M. Misra, S. Kaushal, J. Gaur, S. Kumar and G. Singh, Enhancing Optoelectronic Performance Through Rare-Earth-Doped ZnO: Insights and Applications, *Photonics*, Vol. 12, No. 5, 2025, pp. 454, <https://doi.org/10.3390/photonics12050454>.
- [8] S. Mondal, M. Jamal, S. A. Ayon, M. J. F. Anik, M. M. Billah, Synergistic Enhancement of Photocatalytic and Antimicrobial Efficacy of Nitrogen and Erbium Co-doped ZnO Nanoparticles, *J. Rare Earths*, Vol. 42, No. 5, 2024, pp. 859-868, <https://doi.org/10.1016/j.jre.2023.10.002>.
- [9] D. Dash, N. R. Panda, D. Sahu, Sm^{3+} Driven Enhancement in Photocatalytic Degradation of Hazardous Dyes And Photoluminescence Properties of Hexagonal-ZnO Nanocolumns, *Nano Ex.*, Vol. 2, No. 1, 2021, pp. 010007, <https://doi.org/10.1088/2632-959X/abd90b>.
- [10] B. D. Cullity, S. R. Stock, *Elements of X-Ray Diffraction*, 3rd Ed., Prentice-Hall Inc., ISBN 0-201-61091-4. 2001, pp. 96-102.
- [11] W. L. Bragg, The Reflection of X-rays by Crystals, *Proceedings of the Royal Society of London, Series A*, Vol. 89, No. 611, 1913, pp. 482-493.
- [12] P. V. Korake, A. N. Kadam, K. M. Garadkar, Photocatalytic Activity of Eu^{3+} -doped ZnO Nanorods Synthesized Via Microwave Assisted Technique. *J. Rare Earths*, Vol. 32, No. 4, 2014 pp. 306-313, [https://doi.org/10.1016/S1002-0721\(14\)60072-7](https://doi.org/10.1016/S1002-0721(14)60072-7).

- [13] S. L. Romero, M. J. Q. Jiménez, M. H. García, A. A. Castillo, Bright Red Luminescence and Structural Properties of Eu^{3+} Ion Doped ZnO by Solution Combustion Technique. *World J. Condens. Matter Phys.*, Vol. 4, No. 4, 2014, pp. 227-234, <http://dx.doi.org/10.4236/wjcmp.2014.44024>.
- [14] M. Šćepanović, M. G. Brojčin, K. Vojisavljević, S. Bernik, T. Srećković, Raman Study of Structural Disorder in ZnO Nanopowders, *J. Raman Spectrosc.*, Vol. 41, No. 9, 2010, pp. 914-921, <http://dx.doi.org/10.1002/jrs.2546>.
- [15] Y. Song, S. Zhang, C. Zhang, Y. Yang, K. Lv, Raman Spectra and Microstructure of Zinc Oxide Irradiated with Swift Heavy Ion, *Crystals*, Vol. 9, No. 8, 2019, pp. 395, <https://doi.org/10.3390/cryst9080395>.
- [16] I. Musa, N. Qamhieh, S. T. Mahmoud, Synthesis and Length Dependent Photoluminescence Property of Zinc Oxide Nanorods, *Result. Phys.*, Vol. 7, 2017, pp. 3552-3556, <http://dx.doi.org/10.1016/j.rinp.2017.09.035>.
- [17] A. M. Kasumov, V. V. Strelchuk, O. F. Kolomys, O. I. Bykov, V. O. Yukhymchuk, M. M. Zahornyi, K. A. Korotkov, V. M. Karavaieva, S. F. Korychev, A. I. Ievtushenko, Properties of Nanosized ZnO:Ho Films Deposited Using Explosive Evaporation, *SPQEO*, Vol. 24, No. 2, 2021, pp. 139-147, <https://doi.org/10.15407/spqeo24.02.139>.
- [18] R. Cuscó, E. A. Lladó, J. Ibáñez, L. Artús, J. Jiménez, B. Wang, M. J. Callahan, Temperature Dependence of Raman Scattering in ZnO, *Phys. Rev. B*, Vol. 75, 2007, pp. 165202, <http://dx.doi.org/10.1103/PhysRevB.75.165202>.
- [19] R. L. S. Silva, A. Franco Jr, Raman Spectroscopy Study of Structural Disorder Degree of ZnO Ceramics, *Mater. Sci. Semicond. Process.*, Vol. 119, No. 15, 2020, pp. 105227, <https://doi.org/10.1016/j.mssp.2020.105227.V>.
- [20] R Raji, K. Gopchandran, ZnO Nanostructures with Tunable Visible Luminescence: Effects of Kinetics of Chemical Reduction and Annealing, *Journal of Science: Advanced Materials and Devices*, Vol. 2, 2017, pp. 51-58, <https://doi.org/10.1016/j.jsamd.2017.02.002>.
- [21] C. T. Quy, N. X. Thai, N. D. Hoa, D. T. T. Le, C. M. Hung, N. V. Duy, N. V. Hieu, $\text{C}_2\text{H}_5\text{OH}$ and NO_2 Sensing Properties of ZnO Nanostructures: Correlation between Crystal Size, Defect Level and Sensing Performance, *RSC Adv.*, Vol. 8, No. 10, 2018, pp. 5629-5639, <https://doi.org/10.1039/C7RA13702H>.
- [22] P. K. Upadhyay, N. Sharma, S. Sharma, R. Sharma, Photo and Thermoluminescence of Eu Doped ZnO Nanophosphors, *J. Mater. Sci.: Mater. Electron.*, Vol. 32, 2021, pp. 17080-17093, <https://doi.org/10.1007/s10854-021-06043-w>.
- [23] T. T. T. Huong, N. T. Sa, N. T. M. Thuy, P. V. Hao, N. H. Thao, N. T. Hien, N. X. Ca. Eu^{3+} -doped ZnO Quantum Dots: Structure, Vibration Characteristics, Optical Properties, and Energy Transfer Process, *Nanosc. Adv.*, Vol. 7, No.3, 2025, pp. 909-921, <https://doi.org/10.1039/D4NA00858H>.
- [24] K. S. Babu, A. R.Reddy, C. Sujatha, K. Ve. Reddy, Optimization of UV Emission Intensity of ZnO Nanoparticles by Changing the Excitation Wavelength, *Mater. Lett.*, Vol. 99, No. 15, 2013, pp. 97-100. <https://doi.org/10.1016/j.matlet.2013.02.079>
- [25] C. Picasso, Y. Salinas, O. Brüggemann, M. C. Scharber, N. S. Sariciftci, O. D. F. Cardozo, E. S. Rodrigues, M. S. Silva, A. Stingl and P. M. A. Farias, Lanthanide (Eu, Tb, La)-Doped ZnO Nanoparticles Synthesized Using Whey as an Eco-Friendly Chelating Agent, *J. Nanomater.*, Vol. 12, No. 13, 2022, pp. 2265, <https://doi.org/10.3390/nano12132265>.
- [26] G. Li, G. Cai, X. Wang, Local Structure-Luminescence Correlation in Eu^{3+} -Doped Phosphors: A Comprehensive Review, *Adv. Photonics Res.*, Vol. 6, No. 11, 2025, pp. 2500142, <https://doi.org/10.1002/adpr.202500142>.